AIAA Journal
Vol. 45, No. 9, September 2007

Response of a Flat-Plate Cascade to Incident Vortical Waves

Saad A. Ragab* and Abdel-Halim Salem-Said†
Virginia Polytechnic Institute and State University, Blacksburg, Virginia 24061-0219

DOI: 10.2514/1.26951

In this paper, we are interested in computing the unsteady loading and radiated acoustic pressure field from a flat-plate cascade excited by an incident vortical wave (gust). We solve the two-dimensional nonlinear Euler equations over a linear cascade by a high-order finite difference method. We use Giles's nonreflecting boundary conditions at the inflow and outflow boundaries. The cascade response depends sensitively on the frequency of the convected gust. The unsteady surface pressure distribution and radiated pressure field agree very well with predictions of the linear theory for the tested range of reduced frequency. We also investigate the effects of the incident gust frequency on the undesirable wave reflection at the inflow and outflow boundaries.

Nomenclature

CN = normal force coefficient
c = plate chord
c_1, c_2, c_3, c_4 = one-dimensional characteristic variables
c_∞ = freestream mean speed of sound
E = total specific energy
k_1, k_2 = wave numbers of the gust
L = normal force per unit span
L_x = streamwise domain length
M_∞ = freestream mean Mach number
n_b = number of blades
n_c = number of grid points on the chord
n_s = number of grid points on the pitch
p = pressure
R = gas constant
s = blade-to-blade spacing
T = temperature
T_∞ = freestream mean temperature
t = time
U_∞ = freestream mean velocity
u, v = velocity components
$\tilde{u}, \tilde{v}$ = velocity components of the gust
u_o, v_o = amplitude of velocity components of the gust
x, y = streamwise and transverse coordinates
γ = specific heat ratio
Δp = pressure jump across the plate
Δt = time step
$\Delta x, \Delta y$ = grid spacing in the x and y directions
κ = reduced frequency
ρ = density
ρ_∞ = freestream mean density
ω = gust frequency

I. Introduction

A SIGNIFICANT component of the noise radiated by shrouded propellers and turbofans is due to interactions of ingested turbulence with rotor blades and guide vanes. The incident turbulence is usually generated in boundary layers on surfaces upstream of the propeller, such as the vessel hull, the control surfaces, and the wakes of rotor blades upstream of the guide vanes. It may also be present in the incident freestream due to environmental effects such as atmospheric turbulence or breaking of internal or surface gravity waves. The incident turbulence usually contains large-scale structures with integral length scales comparable to the blade-to-blade spacing or even larger. The interactions of these scales with rotating blades or guide vanes result in pressure fluctuations, unsteady lift, vibrations, and hence noise radiation. Simultaneously, the turbulence length scales, intensities, and wave-number-frequency spectra are significantly modified by the interaction with the blades.

Over the past decade, several models have been proposed for the prediction of propellers and turbofans noise. Majumdar and Peake [1] used rapid distortion theory (RDT) to predict the distortion of ingested freestream turbulence by the strain field of nonuniform mean flow upstream of an open or ducted fan. They assumed that the incident turbulence is given by von Kármán spectrum. They used a strip theory to predict the unsteady forces on rotating fan blades and determined the radiated sound by solving the convected wave equation with the help of Green's function. They found that the distortion of incident turbulence under static (zero forward speed) conditions produced high tonal noise levels, whereas the radiated sound is generally broadband under flight (aircraft approach) conditions.

Atassi et al. [2] examined the effect of mean flow swirl on the acoustic and aerodynamic responses of a set of guide vanes. The swirl is imparted to the incoming flow by a rotor upstream of the guide vanes that are modeled by an unloaded (zero-mean lift) annular cascade. They linearized the Euler equations around a nonuniform mean state and assumed time-harmonic disturbances. Because the disturbance equations have variable coefficients, Atassi et al. used a finite difference method and solved for the flow in a single-blade passage, assuming quasi-periodic conditions in the circumferential direction. They showed that the mean swirl changes the mechanics of the scattering of incident acoustic and vortical disturbances. They pointed to the importance of the radial phase of the incident disturbance in the scattering process.

Because of its simplicity and efficiency, RDT has been extensively used for investigating the interactions of turbulence with blades and for predicting the radiated noise from rotors. Kullar and Graham [3] obtained an integral equation for the loading of a flat-plate linear cascade due to an incident three-dimensional gust composed of an upwash-velocity component superimposed on a uniform stream. They examined the effects of Mach number and three-dimensionality of gust on acoustic resonances between cascade blades. Glegg [4] also obtained an integral equation for the loading (expressed as a jump in the velocity potential across the blades) and solved that equation by the Wiener–Hopf method. He obtained analytical expressions for the unsteady loading, acoustic mode amplitude, and sound power output of the cascade. One of his conclusions is that the

---

Presented as Paper 3231 at the 36th AIAA Fluid Dynamics Conference and Exhibit, San Francisco, CA, 5–8 June 2006; received 1 August 2006; revision received 27 March 2007; accepted for publication 27 March 2007.

*Professor, Engineering Science and Mechanics Department. Member AIAA.

†Ph.D. Student.

primary effect of sweep on the radiated sound power is to cause the propagating acoustic modes to become cut off. This effect depends on the Mach number.

Graham [5] used RDT with simplifying assumptions and obtained analytical solutions for the turbulence spectra downstream of a flat-plate linear cascade. He noted that "…the turbulence flow field for these convective flows is inhomogeneous in the streamwise direction over a distance of order Ł_∞ [integral length scale]. This is the region within which there is a significant pressure field associated with the interaction between the turbulence and the leading edge." Therefore, a simplified RDT in which the turbulence is assumed to be homogeneous in the streamwise direction does not apply in this region. Also, RDT does not apply for streamwise distances much greater than Ł_∞ from the leading edge.

The long-term objective of our research is to develop an efficient computational method for the interaction of large-scale turbulence with propeller and turbofan blades and to predict the associated radiated noise. Salem-Said and Ragab [6] conducted large-eddy simulations of the distortion of homogeneous turbulence by a flat-plate cascade. Their results for the Reynolds stresses and energy spectra downstream of the cascade agree with Graham's RDT theory in its region of validity.

In this paper, we are interested in computing the unsteady lift and radiated sound from a flat-plate cascade due to an incident vortical wave (gust). We solve the two-dimensional nonlinear Euler equations over a linear cascade composed of six plates for a range of discrete frequencies of the incident gust. We use Giles's [7] nonreflecting boundary conditions at the inflow and outflow boundaries and study their performance at different frequencies of the incident gust. These boundary conditions have been also investigated for the cascade problem by Hixon et al. [8] and used by Sawyer et al. [9] for aeroacoustic prediction of rotor–stator interaction noise. Giles's [7] conditions, being based on a Taylor series expansion for a small ratio of tangential wave number to frequency, are approximately nonreflecting. Rowley and Colonius [10] (see also Colonius [11] for a review) developed numerically nonreflecting conditions. Yaguchi and Sugihara [12] also proposed new nonreflecting boundary conditions for multidimensional compressible flow. Prediction of radiated sound by a cascade of blades due to interaction with turbulence can benefit from these new nonreflecting conditions.

II. Mathematical Formulation

A. Euler Equations

We solve the full nonlinear Euler equations in the conservative form on a uniform Cartesian grid:

$$\frac{\partial \rho}{\partial t} + \frac{\partial \rho u_j}{\partial x_j} = 0 \tag{1}$$

$$\frac{\partial \rho u_i}{\partial t} + \frac{\partial (\rho u_i u_j + p\delta_{ij})}{\partial x_j} = 0 \tag{2}$$

$$\frac{\partial \rho E}{\partial t} + \frac{\partial (\rho E + p) u_j}{\partial x_j} = 0 \tag{3}$$

where

$$E = \frac{p}{(\gamma - 1)\rho} + \frac{1}{2} u_i u_i \tag{4}$$

A perfect gas with specific heat ratio $\gamma = 1.4$ is assumed.

$$p = \rho R T \tag{5}$$

B. Finite Difference Method

In the present paper, we use a sixth-order compact finite difference scheme (Lele [13], and Zhong [14]) for spatial derivatives. In the nonperiodic x direction, the scheme is given by

$$\alpha f'_{i-1} + f'_i + \alpha f'_{i+1} = \tfrac{1}{h}[a(f_{i+1} - f_{i-1}) + b(f_{i+2} - f_{i-2})] \tag{6}$$

where $\alpha = 1/3$, $a = 7/9$, $b = 1/36$, and h is the grid step size. This scheme is applied for $i = 3, \ldots, n-2$. Fifth-order explicit schemes (Carpenter et al. [15]) are used at the boundary points $i = 1, 2, n$ and $n-1$:

For $i = 1$:

$$f'_i = \tfrac{1}{h}(\bar{c}_0 f_i + \bar{c}_1 f_{i+1} + \bar{c}_2 f_{i+2} + \bar{c}_3 f_{i+3} + \bar{c}_4 f_{i+4} + \bar{c}_5 f_{i+5} + \bar{c}_6 f_{i+6} + \bar{c}_7 f_{i+7}) \tag{7}$$

$$f'_{i+1} = \tfrac{1}{h}(\bar{e}_0 f_i + \bar{e}_1 f_{i+1} + \bar{e}_2 f_{i+2} + \bar{e}_3 f_{i+3} + \bar{e}_4 f_{i+4} + \bar{e}_5 f_{i+5} + \bar{e}_6 f_{i+6} + \bar{e}_7 f_{i+7}) \tag{8}$$

For $i = n$:

$$f'_i = -\tfrac{1}{h}(\bar{c}_0 f_i + \bar{c}_1 f_{i-1} + \bar{c}_2 f_{i-2} + \bar{c}_3 f_{i-3} + \bar{c}_4 f_{i-4} + \bar{c}_5 f_{i-5} + \bar{c}_6 f_{i-6} + \bar{c}_7 f_{i-7}) \tag{9}$$

$$f'_{i-1} = -\tfrac{1}{h}(\bar{e}_0 f_i + \bar{e}_1 f_{i-1} + \bar{e}_2 f_{i-2} + \bar{e}_3 f_{i-3} + \bar{e}_4 f_{i-4} + \bar{e}_5 f_{i-5} + \bar{e}_6 f_{i-6} + \bar{e}_7 f_{i-7}) \tag{10}$$

The coefficients are given by Carpenter et al. [15]. Because of the singularities at the leading and trailing edges, we do not apply the sixth-order compact scheme at points that straddle these edges on y planes that coincide with the plates. Instead, we use the explicit fifth-order schemes [Eq. (8)] at the points $i = ile + 1$ and $ite + 1$, and we use Eq. (10) at the points $i = ile - 1$ and $i = ite - 1$, where ile and ite are the indices of the leading and trailing edges of the plate, respectively.

The Euler equations are also solved on the upper and lower surfaces of each plate. The Poinsot and Lele [16] slip wall boundary condition is used. The flux vector derivative parallel to the plate (x operator) is evaluated using the sixth-order compact scheme, as shown earlier at the points $ile + 2 \geq i \geq ite - 2$. The derivatives normal to the wall (y direction) are evaluated by a one-sided explicit third-order scheme for velocity v and a first-order scheme for pressure p. The flow variables at the leading and trailing edges are obtained by averaging the solutions at the two nearest field points above and below the edges.

The low-storage, five-stage, fourth-order Runge–Kutta scheme of Carpenter and Kennedy [17] is used to advance the solution in time. The compact sixth-order scheme is nondissipative, and hence a filter is needed to damp dispersed high wave numbers. We use a tenth-order compact spatial filter, as given by Visbal and Gaitonde [18,19]. For the near-boundary points, we use successively lower even-order compact filters, with a filter parameter given by $\alpha_f = 0.5125-0.01125 m_f$, where m_f is the order of the filter; for example, $\alpha_f = 0.40$ for the tenth-order filter, $\alpha_f = 0.4225$ for the eighth-order filter, and so on. The filter is applied to the conservative variables once every time step after the fifth stage of the Runge–Kutta scheme.

C. Boundary Conditions

At the inflow boundary, the incoming flow is composed of two contributions: a uniform flow that is parallel to the plates (U_∞, $V_\infty = 0$, ρ_∞, and p_∞) and a vortical gust with prescribed velocity components $\tilde{u}$ and $\tilde{v}$, but without pressure or density variations. Additional perturbations at the boundary are due to the interaction of the gust with the cascade u', v', ρ', and p'. For the purpose of applying the boundary conditions only, we write

$$u = U_\infty + \tilde{u} + u' \tag{11}$$

$$v = V_\infty + \tilde{v} + v' \tag{12}$$

$$p = p_\infty + p' \tag{13}$$

$$\rho = \rho_\infty + \rho' \tag{14}$$

In developing nonreflection boundary conditions, Giles [7] linearized the 2-D Euler equations about a uniform basic state. The one-dimensional characteristic variables are related to the field perturbations u', v', ρ', and p' by

$$c_1 = p' - \rho_\infty c_\infty u' \tag{15}$$

$$c_2 = c_\infty^2 \rho' - p' \tag{16}$$

$$c_3 = \rho_\infty c_\infty v' \tag{17}$$

$$c_4 = p' + \rho_\infty c_\infty u' \tag{18}$$

At the inflow boundary, we determine the time derivatives of the incoming characteristic variables from Giles's [7] conditions:

$$\frac{\partial c_2}{\partial t} + V_\infty \frac{\partial c_2}{\partial y} = 0 \tag{19}$$

$$\frac{\partial c_3}{\partial t} + V_\infty \frac{\partial c_3}{\partial y} + \frac{1}{2}(U_\infty + c_\infty)\frac{\partial c_4}{\partial y} - \frac{1}{2}(U_\infty - c_\infty)\frac{\partial c_1}{\partial y} = 0 \tag{20}$$

$$\frac{\partial c_4}{\partial t} + V_\infty \frac{\partial c_4}{\partial y} - \frac{1}{2}(U_\infty - c_\infty)\frac{\partial c_3}{\partial y} = 0 \tag{21}$$

where the y derivative is evaluated by a fourth-order central-difference formula. We also determine the time derivative of the outgoing characteristic variable c_1 from

$$\frac{\partial c_1}{\partial t} = -(U_\infty - c_\infty)\left(\frac{\partial p'}{\partial x} - \rho_\infty c_\infty \frac{\partial u'}{\partial x}\right) \tag{22}$$

where the x derivative is evaluated by a fifth-order one-sided explicit scheme (Carpenter et al. [15]) using information within the computational domain. The values of the perturbations and characteristic variables used to evaluate the x and y derivatives are updated at each of the five stages of the Runge–Kutta scheme. As shown by Hixon et al. [8], the time derivative of the characteristic variables can be used to obtain the derivative of the conservative variables on the boundary. We take the time derivative of Eqs. (15–18) and then use the known derivatives of the characteristic variables to determine the derivatives of the fluctuations. To take into account the gust at the inflow, we determine the time derivatives of the conservative variables by

$$\frac{\partial \rho}{\partial t} = \frac{\partial \rho'}{\partial t} \tag{23}$$

$$\frac{\partial \rho u}{\partial t} = u\frac{\partial \rho'}{\partial t} + \rho\left(\frac{\partial u'}{\partial t} + \frac{\partial \tilde{u}}{\partial t}\right) \tag{24}$$

$$\frac{\partial \rho v}{\partial t} = v\frac{\partial \rho'}{\partial t} + \rho\left(\frac{\partial v'}{\partial t} + \frac{\partial \tilde{v}}{\partial t}\right) \tag{25}$$

$$\frac{\partial \rho E}{\partial t} = \frac{1}{\gamma - 1}\frac{\partial p'}{\partial t} + \rho u\left(\frac{\partial u'}{\partial t} + \frac{\partial \tilde{u}}{\partial t}\right) + \rho v\left(\frac{\partial v'}{\partial t} + \frac{\partial \tilde{v}}{\partial t}\right) + \frac{1}{2}(u^2 + v^2)\frac{\partial \rho'}{\partial t} \tag{26}$$

At the outflow boundary, the time derivative of the incoming characteristic are given by

$$\frac{\partial c_1}{\partial t} + v\frac{\partial c_1}{\partial y} + u\frac{\partial c_3}{\partial y} = 0 \tag{27}$$

whereas the changes in the outgoing characteristics c_2, c_3, and c_4 are obtained from information within the computational domain.

III. Results

In the present simulations, we consider an unstaggered six-blade linear cascade, as shown in Fig. 1. The plates have zero thickness and are at zero incidence relative to the mean flow. The blade-to-blade spacing s is $0.806c$, where c is the blade chord. This geometric parameter is motivated by the cascade experiments conducted by Larssen and Devenport [20] (see also Larssen [21]).

The coordinates and flow variables are made nondimensional by using the plate chord c, freestream velocity U_∞, density ρ_∞, and temperature T_∞ as reference values. The reference pressure is $\rho_\infty U_\infty^2$. In this paper, we consider two-dimensional vortical waves only, hence the gust velocity field ($\tilde{u}$ and $\tilde{v}$) is divergence-free; it is given by

$$\tilde{u} = u_o e^{i(k_1 x + k_2 y - \omega t)} + cc \tag{28}$$

$$\tilde{v} = v_o e^{i(k_1 x + k_2 y - \omega t)} + cc \tag{29}$$

where $u_o = -k_2 v_o / k_1$ and $\omega = k_1 U_\infty$. We assume that $k_1 = k_2 = 2\pi n/(s n_b)$, where n is an integer and n_b is the number of blades in the computational domain. In the preceding equations, cc stands for the complex conjugate of the preceding term. All of the results reported here are obtained for $v_o = 0.01 U_\infty$.

A. Glegg's Linearized Potential Flow Solution

Glegg [4] developed a complete solution to the response of a staggered flat-plate cascade to incident 3-D plane waves. He solved the compressible linearized potential flow equation and accounted for the finite chord of the blades. He provided analytical expressions for the unsteady normal force and the upstream and downstream sound power, all as functions of the wave number and frequency of the incident gust and the geometric properties of the cascade. We developed a linear-theory code based on Glegg's analytical solution and checked it by reproducing the normal force and sound power spectra for all of the cases reported in Glegg. We then used the linear code to provide data for comparison with the nonlinear Euler calculations.

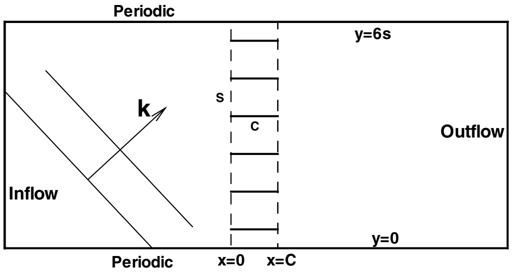

Fig. 1 Flat-plate cascade and computational domain.

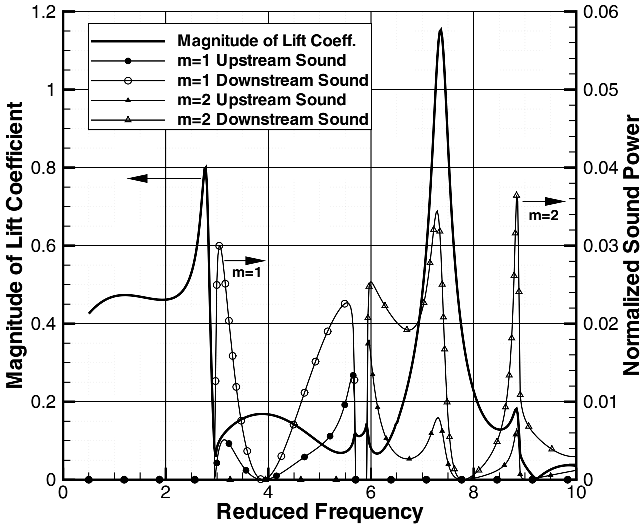

Fig. 2 Unsteady lift response and sound power using Glegg's [4] linear solution at $M_\infty = 0.3$.

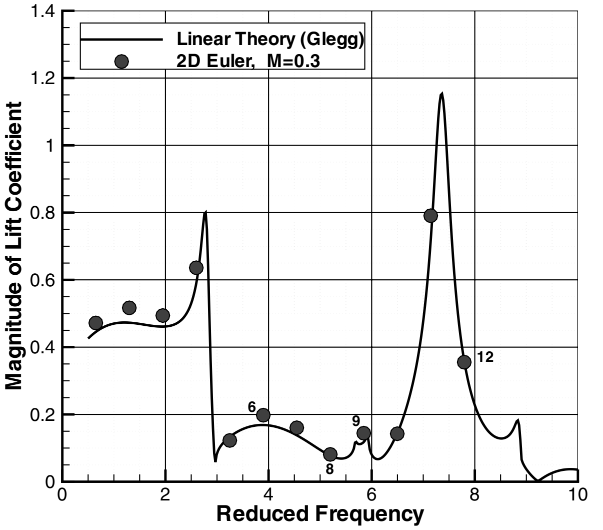

Fig. 4 Comparison of unsteady lift response with Glegg's [4] linear solution at $M_\infty = 0.3$.

Following Glegg [4], we define the normal force coefficient CN by $CN = L/\pi v_o \rho_\infty U_\infty c$, where L is the normal force per unit span, obtained as an integral along the chord of the pressure jump across the plate. The sound power per unit span $W^\pm$ is also normalized by $v_o^2 \rho_\infty U_\infty s n_b/2$. (The upper sign is for upstream radiation and the lower sign is for downstream radiation.) The normal force magnitude and sound power for the cut-on modes at freestream Mach number $M_\infty = 0.3$ as functions of the reduced frequency of the incident gust $\kappa = \omega c/2U_\infty$ are shown in Fig. 2. The second ($m = 1$) and third ($m = 2$) acoustic modes are cut on, each over a range of frequencies, but they do not overlap. There is a small window of frequencies in which both modes are cut off ($\kappa = 5.70125$ to 5.915); the frequency for wave number $n = 9$ is $\kappa = 5.8466$, which falls in that window. Upstream sound power is less than the downstream sound power. The normal force and sound power results at $M_\infty = 0.5$ are depicted in Fig. 3.

B. Two-Dimensional Euler Simulations

We integrated the unsteady two-dimensional nonlinear Euler equations in time on a Cartesian uniform grid. First, we present the unsteady lift spectrum for a range of frequencies of the incident gust. We obtained numerical solutions for 12 separate runs corresponding to $n = 1, 2, \ldots, 12$. In each run, the normal force on each of the six plates was computed by integrating the pressure jump on the plate and its time history was recorded. Excluding a transient period, we decomposed the normal force coefficient into Fourier modes in time. The magnitude of the mode for which the frequency is equal to the gust frequency was averaged over the six plates. The spectrum of the obtained normal force magnitude is depicted in Figs. 4 and 5 at the two Mach numbers $M_\infty = 0.3$ and 0.5, respectively. Overall, the agreement between the present Euler calculations and Glegg's [4] linear solution is very good. The sensitivity of the surface pressure distribution to grid resolution and domain length will be discussed next.

We investigate in more detail the pressure field and excited acoustic modes for three frequencies corresponding to $n = 11$, 8 and 9 at Mach number $M_\infty = 0.3$. As we shall see, each frequency results in a qualitatively different cascade response. We use five grids, as shown in Table 1. Grids A, B, C, and D are used to evaluate sensitivity to the step sizes $\Delta x = \Delta y$, whereas grids C, E, and F are used for sensitivity to the streamwise extent of the computational domain. In this table, n_s and n_c are the number of points on the cascade pitch s and on the plate chord c, respectively. L_x is the streamwise extent of the computational domain and Δt is the time step.

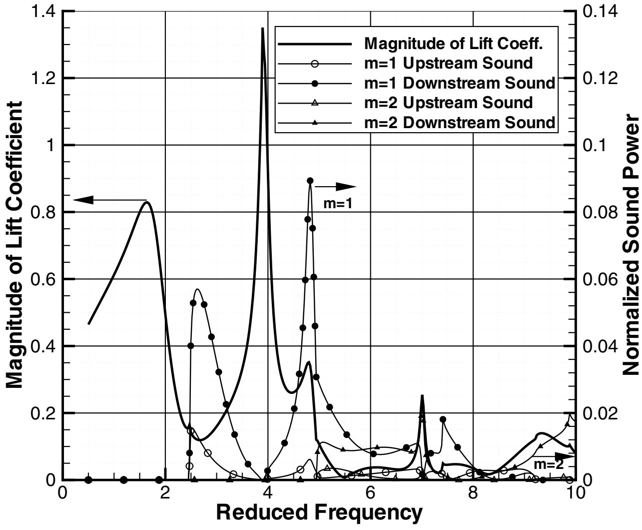

Fig. 3 Unsteady lift response and sound power using Glegg's [4] linear solution at $M_\infty = 0.5$.

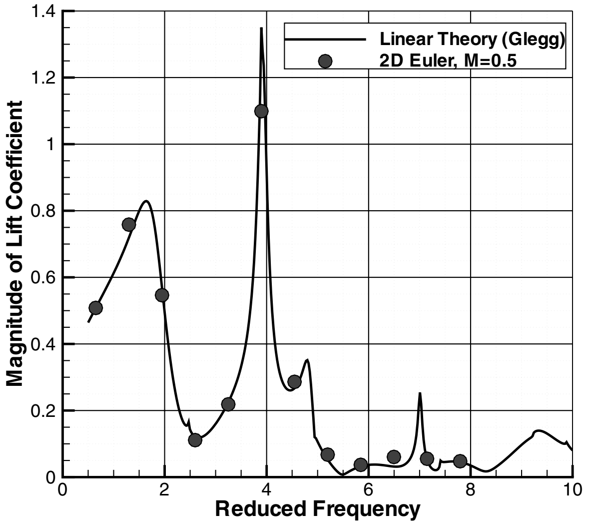

Fig. 5 Comparison of unsteady lift response with Glegg's [4] linear solution at $M_\infty = 0.5$.

Table 1 Grid parameters for test cases 1–3

Grid	n_s	n_c	L_x	Δt
A	25	31	5.0375	0.4198×10^{-2}
B	49	61	5.0375	0.2099×10^{-2}
C	97	120	5.0375	0.1049×10^{-2}
D	193	239	5.0375	0.5247×10^{-3}
E	97	120	7.0525	0.1049×10^{-2}
F	97	120	9.0675	0.1049×10^{-2}

Test Case 1: $n = 11$

A snapshot of pressure contours ($p - 1/\gamma M_\infty^2$) for incident gust with mode number $n = 11$ is shown in Fig. 6. For this gust, the reduced frequency is $\kappa = 7.146$, for which the third acoustic mode is cut on. Pressure fluctuations propagate toward the lower left corner upstream of the cascade and toward the lower right corner downstream of the cascade. We decompose the pressure field $p(x, y, t)$ into a double Fourier series in y and t; each mode is of the general form

$$\tilde{p}(x, k_\nu, \omega_l) = \hat{p}_{l\nu}(x) e^{-i\omega_l t + i\nu k_2 y} \tag{30}$$

The cascade response at the forcing frequency $\omega_l = \omega$ includes only one propagating mode $\nu = -1$, as shown in Fig. 2. The amplitude $|\hat{p}_{l\nu}(x)|$ for this mode is depicted in Fig. 7 upstream of the leading edge and downstream of the trailing edge for the four grids A, B, C, and D. The upstream radiated pressure agrees very well with predictions using Glegg's [4] linear theory. Reflection from the inflow boundary is negligible. As we refine the grid, downstream radiation converges to the linear-theory prediction. However, a small wave reflection from the outflow boundary is evident by the weak variation in the wave amplitude. In addition to the propagating mode $\nu = -1$, there are other modes that decay exponentially upstream and downstream of the cascade. The dominant exponentially decaying mode is $\nu = -7$, which is also depicted in Fig. 7. This mode shows very little sensitivity to grid resolution and is not influenced by reflection from the inflow or outflow boundaries.

The pressure jump across a plate $\Delta p(x, t)$ is decomposed into Fourier series in time, of which a mode is

$$\widetilde{\Delta p}(x, \omega_l) = \widehat{\Delta p}_l(x) e^{-i\omega_l t} \tag{31}$$

At the gust frequency $\omega_l = \omega$, the real and imaginary parts of $\widehat{\Delta p}_l(x)$ are compared with predictions of Glegg's [4] linear theory in Fig. 8 for grids A, B, C, and D; grid convergence is also shown. We note here that the coarse grid A gives 13 points per wavelength, whereas the fine grid D gives 105 points. The singularity in $\Delta p(x, t)$ at the leading edge is difficult to resolve; nevertheless, the predicted pressure distribution varies smoothly there. Near the trailing edge, we also see a small glitch in the pressure. Sensitivity of the surface pressure distribution to the extent of the computational domain in the streamwise direction is a good indicator of the reflections from the inflow and outflow boundaries. With the leading edge at $x = 0$, the inflow boundary is placed at $x = -2$, -3, and -4 for the three grids C, E, and F, respectively. The domain length L_x is given in Table 1. The surface pressure distributions for the three domains are shown in Fig. 9, along with the linear-theory prediction. For this frequency, the effects of the domain length are negligible. Reflection from the boundaries is negligible, because the wave-number vector of the excited acoustic mode makes a small angle with the normal to the boundary, which is the right condition for the application of Giles's [7] nonreflecting boundary conditions.

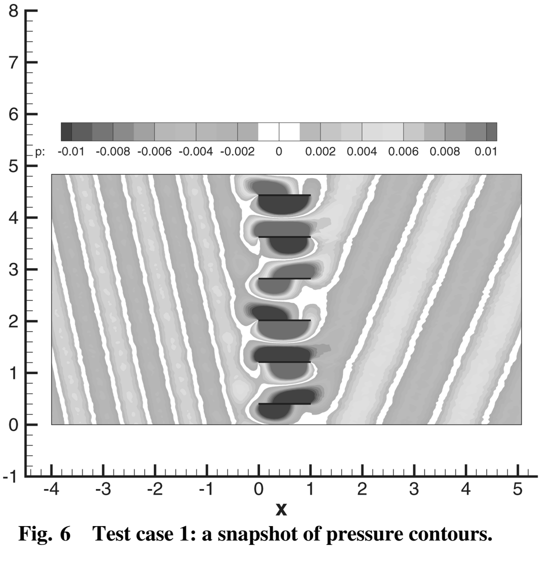

Fig. 6 Test case 1: a snapshot of pressure contours.

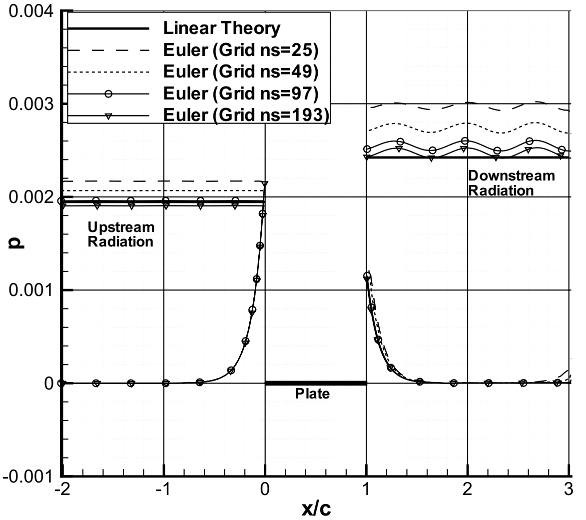

Fig. 7 Test case 1: pressure amplitudes for propagating mode $\nu = -1$ and decaying mode $\nu = -7$.

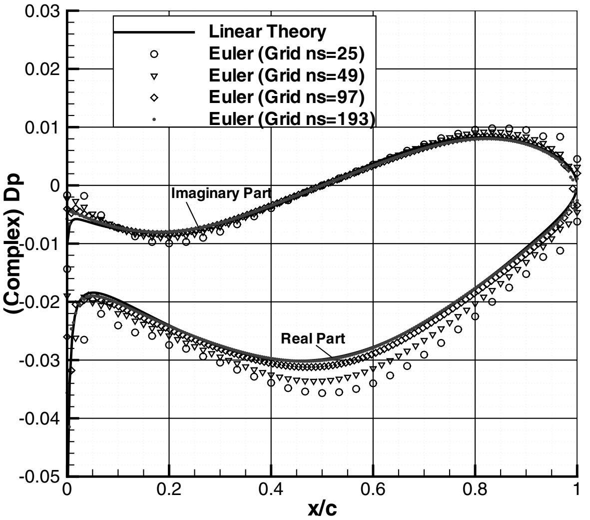

Fig. 8 Test case 1: sensitivity of surface pressure jump to grid step sizes.

Test Case 2: $n = 8$

A snapshot of pressure contours is shown in Fig. 10 for incident gust with mode number $n = 8$. (Because the domain of six blades includes two wavelengths in the y direction, only half of the domain is shown in the figure.) For this gust, the reduced frequency is $\kappa = 5.197$, for which the second acoustic mode is cut on. Upstream of the cascade, pressure fluctuations propagate toward the upper left corner, and downstream of the cascade, they propagate toward the upper right corner. Reflection from the outflow boundary is evident and is more significant than from that at the inflow boundary. This is

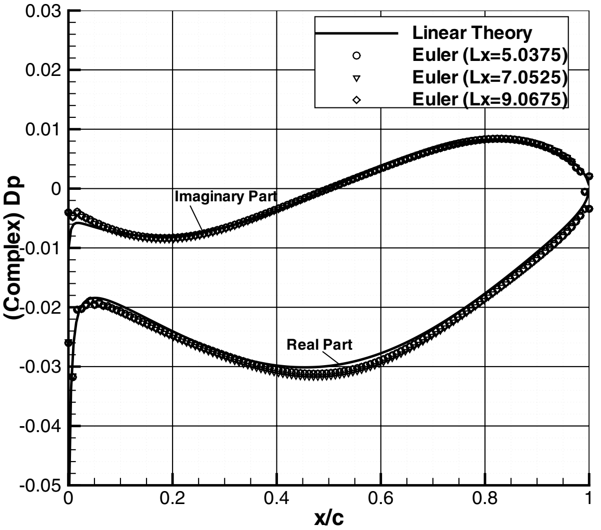

Fig. 9 Test case 1: sensitivity of surface pressure jump to streamwise domain length.

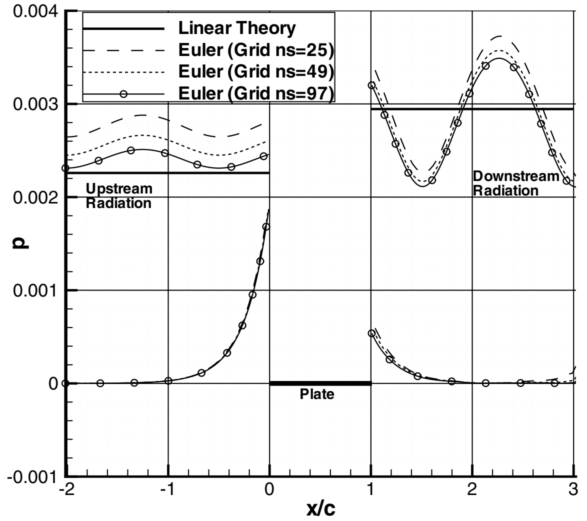

Fig. 11 Test case 2: pressure amplitudes for propagating mode $\nu = 2$ and decaying mode $\nu = -4$.

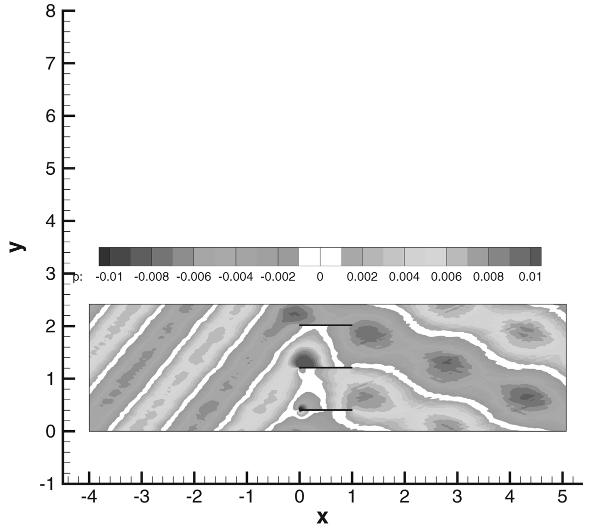

Fig. 10 Test case 2: a snapshot of pressure contours.

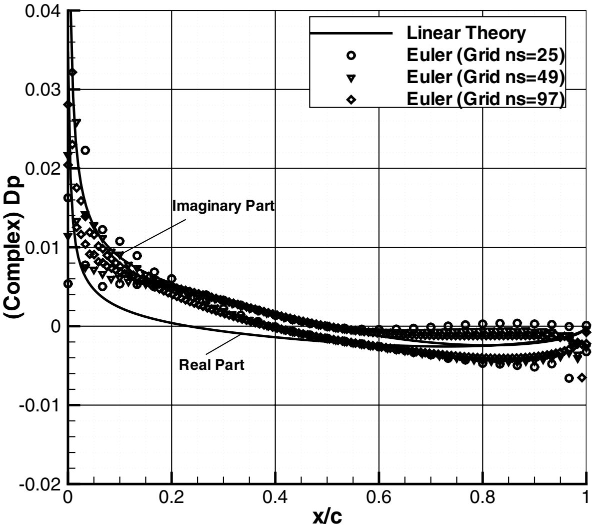

Fig. 12 Test case 2: sensitivity of surface pressure jump to grid step sizes.

because the wave-number vector has a larger tangential component at outflow. Reflection from the outflow boundary contaminates the pressure field, causing significant dependence of the surface pressure distribution on the locations of the inflow and outflow boundaries.

The cascade response at the forcing frequency $\omega_l = \omega$ includes only one propagating mode: $\nu = 2$. The amplitude $|\hat{p}_{l\nu}(x)|$ of radiated pressure for this mode is depicted in Fig. 11 upstream of the leading edge and downstream of the trailing edge for the three grids A, B, and C. With grid refinements, the upstream radiated pressure converges to the predictions using Glegg's [4] linear theory. The undulations in the pressure amplitude are about 5% of the mean value. However, stronger undulations are observed for the downstream radiated wave, because of reflection from the outflow boundary. (Because of the significant reflection from the downstream boundary, we felt that it is not necessary to obtain results for the finest grid D.) In addition to the propagating mode $\nu = 2$, there are other modes that decay exponentially upstream and downstream of the cascade. The dominant exponentially decaying mode is $\nu = -4$, which is also depicted in Fig. 11. This mode shows very little sensitivity to grid resolution and is not influenced by reflection from the inflow or outflow boundaries.

At the gust frequency $\omega_l = \omega$, the real and imaginary parts of surface pressure jump $\widehat{\Delta p_l}(x)$ are compared with predictions of Glegg's [4] linear theory in Fig. 12 for grids A, B, and C. Comparison with linear-theory predictions is poor, and as shown in Fig. 13, the surface pressure distribution is very sensitive to the locations of the inflow and outflow boundaries. In this case, $n = 8$ reflection from the boundaries is significant, because the wave-number vector makes a large angle with the normal to the boundary, for which Giles's [7] nonreflecting boundary conditions break down, especially at the outflow boundary. This is a challenging case for nonreflecting boundary conditions.

Test Case 3: $n = 9$

Pressure contours for incident gust with mode number $n = 9$ are shown in Fig. 14. (Because the domain of six blades includes three wavelengths in the y direction, only one third of the domain is shown in the figure.) For this gust, the reduced frequency is $\kappa = 5.8466$, which falls in the frequency range in which no acoustic mode is cut on, as shown in Fig. 2. Pressure fluctuations are given by standing waves that are dominant in the near field and decay exponentially upstream and downstream of the cascade. The pressure field exhibits a node at $x = 0.428$ from the plate leading edge.

At the gust frequency $\omega_l = \omega$, the real and imaginary parts of surface pressure jump $\widehat{\Delta p_l}(x)$ are compared with predictions of Glegg's [4] linear theory in Fig. 15 for grids A, B, C, and D. Grid

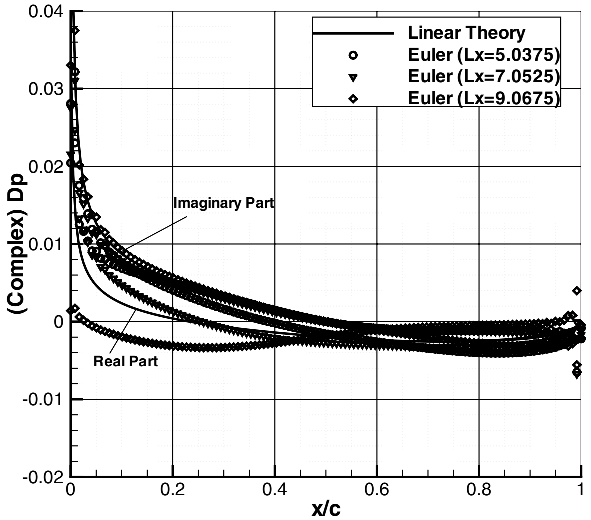

Fig. 13 Test case 2: sensitivity of surface pressure jump to streamwise domain length.

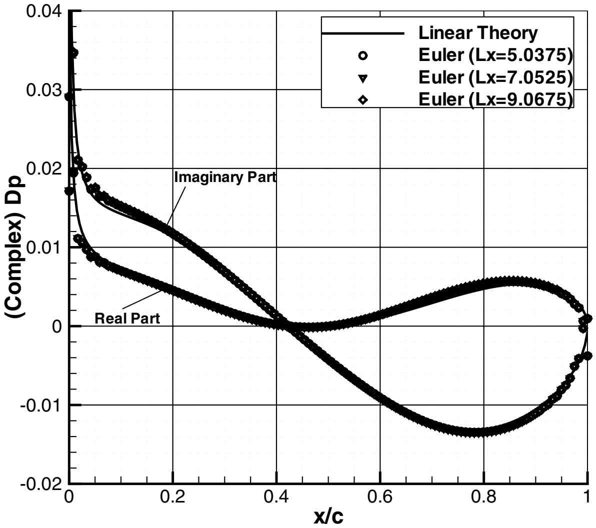

Fig. 16 Test case 3: sensitivity of surface pressure jump to streamwise domain length.

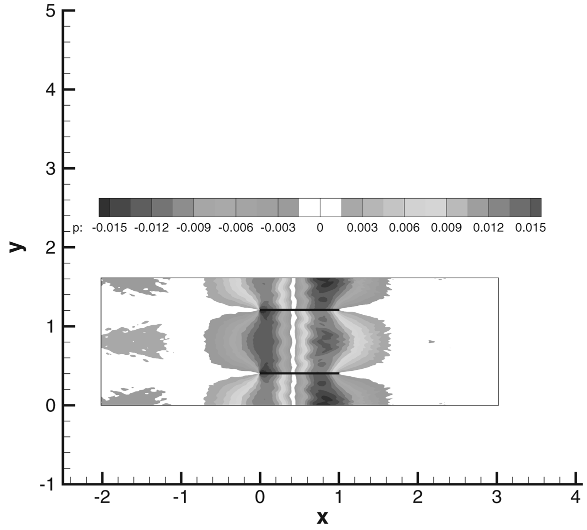

Fig. 14 Test case 3: a snapshot of pressure contours.

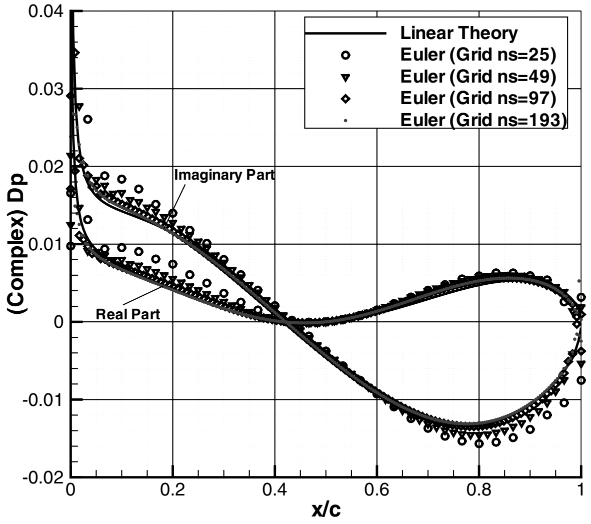

Fig. 15 Test case 3: sensitivity of surface pressure jump to grid step sizes.

convergence is shown, and excellent agreement with the linear theory is obtained. The surface pressure distributions for different domain lengths are shown in Fig. 16, along with the linear-theory prediction. It is evident that the effects of the domain length are negligible.

Test Case 4: $n = 5$

Next, we present results for the benchmark problem considered by Hixon et al. [8]. The cascade is made of four blades with pitch $s = 1$. The convected vortical gust is given by Eqs. (28) and (29) for $n = 5$, and the Mach number is $M_\infty = 0.5$. Table 2 gives the parameters for the five grids used to investigate sensitivity to step sizes and domain length.

A snapshot of pressure contours is shown in Fig. 17. For this gust, the reduced frequency is $\kappa = 7.854$, for which the second acoustic mode is cut on. Upstream of the cascade, pressure fluctuations propagate toward the upper left corner, and downstream of the cascade, they propagate toward the upper right corner. The cascade response at the forcing frequency $\omega_l = \omega$ includes only one propagating mode: $\nu = 1$. The amplitude $|\hat{p}_{l\nu}(x)|$ for this mode is depicted in Fig. 18 upstream of the leading edge and downstream of the trailing edge for the four grids A, B, C, and D. The upstream radiated pressure is 5% higher than that predicted by using Glegg's [4] linear theory. Reflection from the inflow boundary is negligible. As we refine the grid, downstream radiation converges to the linear-theory prediction. However, the weak undulations in the wave amplitude indicate a small wave reflection from the outflow boundary. In addition to the propagating mode $\nu = 1$, there are other modes that decay exponentially upstream and downstream of the cascade. The dominant exponentially decaying mode is $\nu = -3$, which is also depicted in Fig. 18. This mode shows very little sensitivity to grid resolution and is not influenced by reflection from the inflow or outflow boundaries. It dominates the radiated pressure in the near field.

Table 2 Grid parameters for test case 4

Grid	n_s	n_c	L_x	Δt
A	25	25	5	0.6173×10^{-2}
B	49	49	5	0.3086×10^{-2}
C	97	97	5	0.1543×10^{-2}
D	193	193	5	0.7716×10^{-3}
E	97	97	7	0.1543×10^{-2}
F	97	97	9	0.1543×10^{-2}

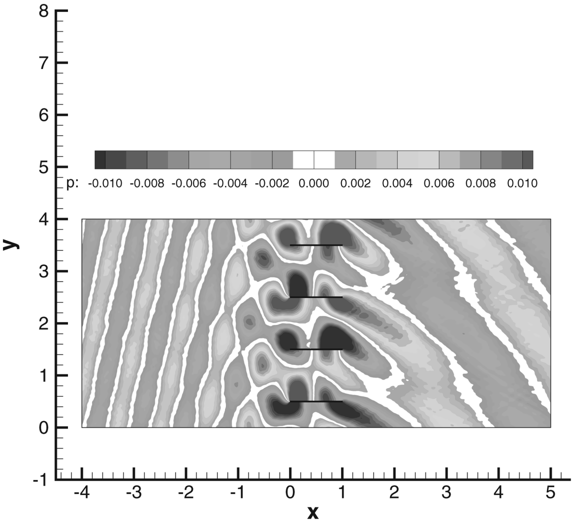

Fig. 17 Test case 4: a snapshot of pressure contours.

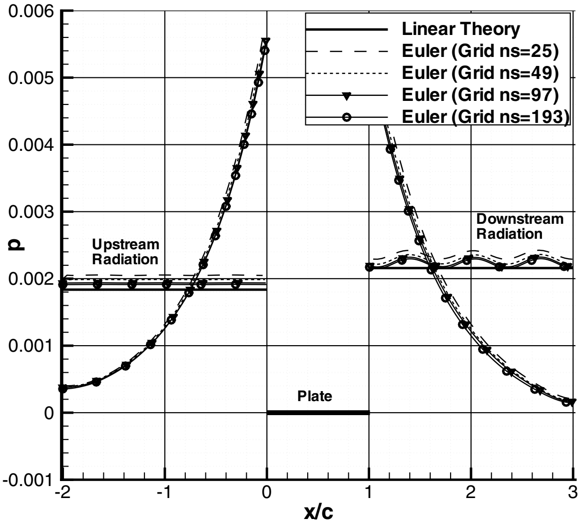

Fig. 18 Test case 4: pressure amplitudes for propagating mode $\nu = 1$ and decaying mode $\nu = -3$.

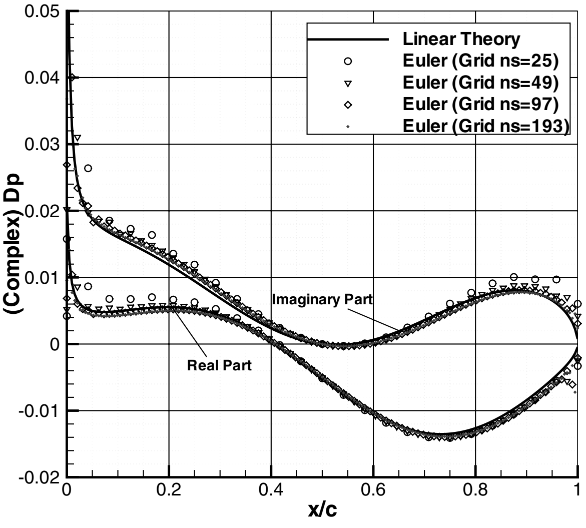

Fig. 19 Test case 4: sensitivity of surface pressure jump to grid step sizes.

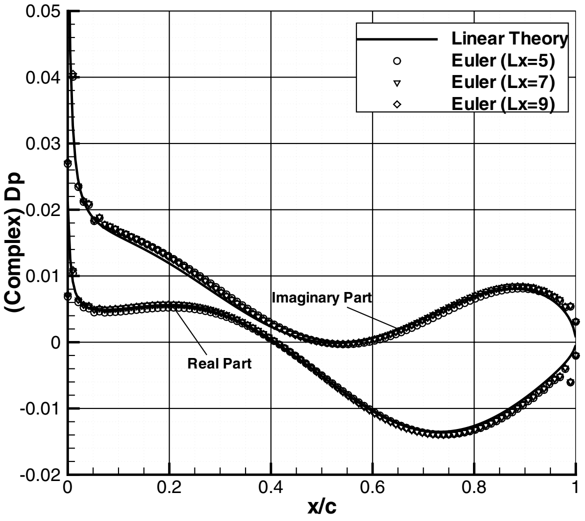

Fig. 20 Test case 4: sensitivity of surface pressure jump to streamwise domain length.

At the gust frequency $\omega_l = \omega$, the real and imaginary parts of $\widehat{\Delta p_l}(x)$ are compared with predictions of Glegg's [4] linear theory in Fig. 19 for grids A, B, C, and D; grid convergence is also shown. Sensitivity of surface pressure distributions to domain length is shown in Fig. 20 for the grids C, E, and F, and, as shown, the effects of the domain length are negligible. In this case, reflection from the boundaries is much smaller than that in case 2.

The streamwise wave numbers for the acoustic waves radiated upstream (k_x^+) and downstream (k_x^-) are shown in Table 3. Also shown is $cos\theta^{\pm}$, where θ is the angle that the wave-number vector makes with the outward normal to the boundary. The outflow boundary in case 2 (for which $\cos\theta^- = 0.375$) suffers the most wave reflection that we have shown, and it calls for applications of higher-order nonreflecting boundary conditions such as those developed by Hagstrom and Goodrich [22].

Conclusions

We considered the response of a flat-plate cascade to two-dimensional vortical waves (gust). We solved the two-dimensional nonlinear Euler equations over a linear cascade composed of six plates for a range of frequencies of the incident gust. The cascade is unstaggered and the pitch-to-chord ratio is 0.806. We use Giles's [7] nonreflecting boundary conditions at the inflow and outflow boundaries. We analyzed the cascade response in terms of unsteady normal force, surface pressure distribution, and radiated acoustic pressure field for three discrete frequencies of the incident gust.

The lift spectrum agrees very well with Glegg's [4] solution to the linearized potential flow equation for the tested range of reduced frequency ($0 < \omega c/2U_\infty < 8$). Because Giles's [7] boundary conditions are approximately nonreflecting, we have investigated undesirable wave reflection at the inflow and outflow boundaries and its variation with gust frequency. Certain frequencies excite acoustic modes for which the wave-number vectors are nearly normal to the boundary. In such cases, minor reflection at the boundary is obtained and the results are insensitive to the location of the computational domain boundaries (cases 1 and 4 of this paper). Other frequencies may still excite acoustic modes for which the wave-number vectors deviate considerably from the normal direction to the boundary,

Table 3 Wave numbers for upstream and downstream propagating modes

Case	n	ν	k_y	k_x^+	k_x^-	$\cos\theta^+$	$\cos\theta^-$
1	11	−1	−1.299	−5.924	3.097	0.977	0.922
2	8	2	2.599	−3.107	1.051	0.642	0.375
4	5	1	1.571	−7.530	2.294	0.979	0.825

resulting in major reflection that contaminates the pressure field (case 2). In such a case, the numerical solution depends sensitively on the locations of the inflow/outflow boundaries. If the gust frequency is such that all acoustic modes are cut off, the pressure field decays exponentially toward the boundaries, and boundary treatment poses no problem (case 3). These observations are consistent with the basic assumption in Giles's derivation of the approximately nonreflecting boundary conditions, which is based on a Taylor series expansion for a small ratio of tangential wave number to frequency. Rowley and Colonius [10] (see also Colonius [11] for a review) and Hagstrom and Goodrich [22] have developed more accurate numerically nonreflecting conditions. Prediction of radiated sound by a cascade of blades due to interaction with turbulence that includes a spectrum of frequencies can greatly benefit from these new nonreflecting boundary conditions.

References

[1] Majumdar, S. J., and Peake, N., "Noise Generation by the Interaction Between Ingested Turbulence and a Rotating Fan," *Journal of Fluid Mechanics*, Vol. 359, Mar. 1998, pp. 181–216.

[2] Atassi, H. M., Ali, A. A., Atassi, O. V., and vin Ogradov, I. V., "Scattering of Incident Disturbances by an Annular Cascade in a Swirling Flow," *Journal of Fluid Mechanics*, Vol. 499, Jan. 2004, pp. 111–138.

[3] Kullar, I., and Graham, J. M. R., "Acoustic Effects Due to Turbulence Passing Through Cascades of Thin Aerofoils," *Journal of Sound and Vibration*, Vol. 110, No. 1, 1985, pp. 143–160.

[4] Glegg, S. A., "The Response of a Swept Blade Row to a Three-Dimensional Gust," *Journal of Sound and Vibration*, Vol. 227, No. 1, 1999, pp. 29–64.

[5] Graham, J. M. R., "The Effect of a Two-Dimensional Cascade of Thin Streamwise Plates on Homogeneous Turbulence," *Journal of Fluid Mechanics*, Vol. 356, Feb. 1998, pp. 125–147.

[6] Salem-Said, A., and Ragab, S. A., "Large Eddy Simulation of the Interaction of Homogeneous Turbulence with a Flat-Plate Cascade," 44th Aerospace Sciences Meeting, Reno, NV, AIAA Paper 2006-1100, 2006.

[7] Giles, M. B., "Nonreflecting Boundary Conditions for Euler Equation Calculations," *AIAA Journal*, Vol. 28, No. 12, 1990, pp. 2050–2058.

[8] Hixon, R., Shih, S.-H., and Mankbadi, R. R., "Evaluation of Boundary Conditions for the Gust-Cascade Problem," *Journal of Propulsion and Power*, Vol. 16, No. 1, 2000, pp. 72–78.

[9] Sawyer, S., Nallasamy, M., Hixon, R., and Dyson, R. W., "A Computational Aeroacoustic Prediction of Discrete-Frequency rotor–stator Interaction Noise—A Linear Theory Analysis," *International Journal of Aeroacoustics*, Vol. 3, No. 1, 2004, pp. 67–86.

[10] Rowley, C. W., and Colonius, T., "Discretely Nonreflecting Boundary Conditions for Linear Hyperbolic Systems," *Journal of Computational Physics*, Vol. 157, No. 2, Jan. 2000, pp. 500–538.

[11] Colonius, T., "Modeling Artificial Boundary Conditions for Compressible Flow," *Annual Review of Fluid Mechanics*, Vol. 36, 2004, pp. 315–345.

[12] Yaguchi, T., and Sugihara, K., "A New Characteristic Nonreflecting Boundary Condition for the Multidimensional Navier-Stokes Equations," 26th AIAA Aeroacoustics Conference, Monterey, CA, AIAA Paper 2005-2868, 2005.

[13] Lele, S. K., "Compact Finite Difference Schemes with Spectral-Like Resolution," *Journal of Computational Physics*, Vol. 103, No. 1, 1992, pp. 16–42.

[14] Zhong, X., "High-Order Finite Difference Schemes for Numerical Simulation of Hypersonic Boundary-Layer Transition," *Journal of Computational Physics*, Vol. 144, No. 2, Aug. 1998, pp. 662–707.

[15] Carpenter, M. H., Gottlieb, D., and Abarbanel, S., "The Stability of Numerical Boundary Treatments for Compact High-Order Finite-Difference Schemes," *Journal of Computational Physics*, Vol. 108, No. 2, 1993, pp. 272–295.

[16] Poinsot, T. J., and Lele, S. K., "Boundary Conditions for Direct Simulations of Compressible Viscous Flows," *Journal of Computational Physics*, Vol. 101, No. 1, 1992, pp. 104–129.

[17] Carpenter, M. H., and Kennedy, C. A., "Fourth-Order, 2N-Storage Runge–Kutta Schemes," NASA Langley Research Center, TM 109112, Hampton, VA, 1994.

[18] Visbal, M. R., and Gaitonde, D., "High-Order-Accurate Methods for Complex Unsteady Subsonic Flows," *AIAA Journal*, Vol. 37, No. 10, 1999, pp. 1231–1239.

[19] Visbal, M. R., and Gaitonde, D., "On the Use of High-Order Finite Difference Schemes on Curvilinear and Deforming Meshes," *Journal of Computational Physics*, Vol. 181, No. 1, 2002, pp. 155–185.

[20] Larssen, J. V., and Devenport, W. J., "Interaction of Large Scale Homogeneous Turbulence with a Cascade of Flat Plates," 41st Aerospace Sciences Meeting, Reno, NV, AIAA Paper 2003-0424, 2003.

[21] Larssen, J. V., "Large Scale Homogeneous Turbulence and Interactions with a Flat-Plate Cascade," Ph.D. Dissertation, Virginia Tech, Blacksburg, VA, 2005.

[22] Hagstrom, T., and Goodrich, J., "Accurate Radiation Boundary Conditions for the Linearized Euler Equations in Cartesian Domains," *SIAM Journal on Scientific Computing*, Vol. 24, No. 3, 2002, pp. 770–7795.

X. Zhong
Associate Editor